AFRL-RX-WP-TP-2008-4339

NUMERICAL AND ANALYTICAL MODELING OF LASER DEPOSITION WITH PREHEATING (PREPRINT)

Zhiqiang Fan, Jacquelyn K. Stroble, Jianzhong Ruan, Todd E. Sparks, and Frank Liou

University of Missouri-Rolla

MARCH 2007

STINFO COPY

AIR FORCE RESEARCH LABORATORY
MATERIALS AND MANUFACTURING DIRECTORATE
WRIGHT-PATTERSON AIR FORCE BASE, OH 45433-7750
AIR FORCE MATERIEL COMMAND
UNITED STATES AIR FORCE

REPORT DOCUMENTATION PAGE

Form Approved
OMB No. 0704-0188

1. REPORT DATE *(DD-MM-YY)*	2. REPORT TYPE	3. DATES COVERED *(From - To)*
March 2007	Conference Paper Preprint	

4. TITLE AND SUBTITLE

NUMERICAL AND ANALYTICAL MODELING OF LASER DEPOSITION WITH PREHEATING (PREPRINT)

5a. CONTRACT NUMBER
FA8650-04-C-5704

5b. GRANT NUMBER

5c. PROGRAM ELEMENT NUMBER
78011F

6. AUTHOR(S)

Zhiqiang Fan, Jacquelyn K. Stroble, Jianzhong Ruan, Todd E. Sparks, and Frank Liou

5d. PROJECT NUMBER
2865

5e. TASK NUMBER
25

5f. WORK UNIT NUMBER
25100000

7. PERFORMING ORGANIZATION NAME(S) AND ADDRESS(ES)

University of Missouri-Rolla
1870 Miner Circle
Rolla, MO 65409-0970

8. PERFORMING ORGANIZATION REPORT NUMBER

9. SPONSORING/MONITORING AGENCY NAME(S) AND ADDRESS(ES)

Air Force Research Laboratory
Materials and Manufacturing Directorate
Wright-Patterson Air Force Base, OH 45433-7750
Air Force Materiel Command
United States Air Force

10. SPONSORING/MONITORING AGENCY ACRONYM(S)

AFRL/RXLMP

11. SPONSORING/MONITORING AGENCY REPORT NUMBER(S)
AFRL-RX-WP-TP-2008-4339

12. DISTRIBUTION/AVAILABILITY STATEMENT
Approved for public release; distribution unlimited.

13. SUPPLEMENTARY NOTES

14. ABSTRACT
Laser deposition allows quick fabrication of fully-dense metallic components directly from CAD solid models. This work uses both numerical and analytical approaches to model the laser deposition process including actual deposition and preheating. The numerical approach is used to simulate the coupled, interactive transport phenomena during actual deposition. The numerical simulation involves laser material interaction, free surface evolution, and melt-pool dynamics. The analytical approach is used to model heat transfer during preheating. The combination of these two approaches can increase computational efficiency with most of the phenomena associated with laser deposition modeled. The simulation is applied to Ti-6Al-4V and simulation results are compared with experimental results.

15. SUBJECT TERMS
laser deposition, CAD, numerical modeling, analytical modeling, preheating, Ti-6Al-4V

16. SECURITY CLASSIFICATION OF:			17. LIMITATION OF ABSTRACT:	18. NUMBER OF PAGES	19a. NAME OF RESPONSIBLE PERSON (Monitor)
a. REPORT	**b. ABSTRACT**	**c. THIS PAGE**	SAR	24	Todd J. Turner
Unclassified	Unclassified	Unclassified			**19b. TELEPHONE NUMBER** *(Include Area Code)* N/A

Standard Form 298 (Rev. 8-98)
Prescribed by ANSI Std. Z39-18

Numerical and Analytical Modeling of Laser Deposition with Preheating

Zhiqiang Fan, Jacquelyn K. Stroble, Jianzhong Ruan, Todd E. Sparks, and Frank Liou

Department of Mechanical and Aerospace Engineering, University Of Missouri–Rolla

1870 Miner Circle, Rolla, MO 65409

Abstract

Laser deposition allows quick fabrication of fully-dense metallic components directly from CAD solid models. This work uses both numerical and analytical approaches to model the laser deposition process including actual deposition and preheating. The numerical approach is used to simulate the coupled, interactive transport phenomena during actual deposition. The numerical simulation involves laser material interaction, free surface evolution, and melt-pool dynamics. The analytical approach is used to model heat transfer during preheating. The combination of these two approaches can increase computational efficiency with most of the phenomena associated with laser deposition modeled. The simulation is applied to Ti-6Al-4V and simulation results are compared with experimental results.

1. Introduction

Laser deposition is an extension of the laser cladding process. This laser additive manufacturing technique allows quick fabrication of fully-dense metallic components directly from Computer Aided Design (CAD) solid models. The applications of laser deposition include rapid prototyping, rapid tooling and part refurbishment. As shown in Fig. 1, laser deposition uses a focused laser beam as a heat source to create a melt pool on an underlying substrate. Powder material is then injected into the melt pool through nozzles. The incoming powder is metallurgically bonded with the substrate upon solidification. The part is fabricated in a layer by layer manner in a shape that is dictated by the CAD solid model.
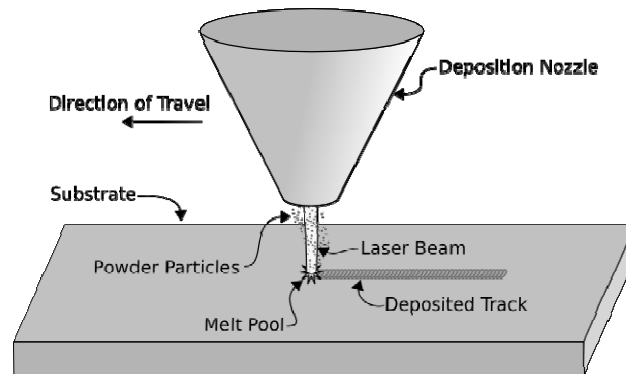
Fig. 1. Schematic of a typical laser deposition system

During the laser deposition process, several defects, such as porosity and cracks, should be paid attention to. Cracks initiate corrosion fracture and reduce fatigue strength of the deposited parts. Cracks are caused by the residual stresses created by the high thermal gradient built up during the cooling stage. Residual stresses can be reduced by a reduction of the cooling rate. This can be achieved by preheating the substrate. Moreover, the preheating causes a better absorption of the laser beam and further it is possible to melt more powder in the larger melting pool and enhance the bonding. Usually the preheating is performed in such a manner that a very small melting of the substrate material occurs without powder injection.

Thermal analysis of the laser deposition process is very important for optimization of the process. If the substrate surface temperatures remain too low, wetted deposit material is limited. In that case, irregularly shaped tracks with a lot of cracks, porosity and a poor bonding, are produced. However, if too high substrate surface temperatures are reached, severe melting of the substrate occurs. The high degree of dilution can deteriorate the clad properties. A comprehensive numerical model has been developed that allows the prediction of temperature distribution and melt pool dynamics. This model simulate the coaxial laser deposition process with powder injection, and considers most of the associated phenomena, such as melting, solidification, evaporation, evolution of the free surface, and powder injection. Input parameters for this model are laser machining parameters and properties of the laser beam, as well as material properties and the laser beam absorption. To get more accurate predictions, finer grid needs to be used. This, together with the iterative nature of the numerical

algorithms, causes the model computationally not very efficient. In this paper an analytical model is applied to the preheating process (without powder injection) to increase the computational efficiency, while the actual deposition process with powder injection still uses the numerical model. The outputs, the temperature distribution of the substrate, are used as the initial conditions of the numerical model.

In this study, a coaxial diode laser deposition system, LAMP (developed at UMR), is considered for simulations and experiments. The blown powder method is used to deliver powder. As the primary laser in the LAMP system, the diode laser is believed to have a number of process advantages as opposed to the CO_2 or Nd:YAG laser, including the better material coupling efficiency (laser absorption) and better beam profile (non Gauss-shape intensity distribution) for laser deposition. Material of both powder and substrates is Ti-6Al-4V, which is widely used in the aerospace industry.

The rest of the paper is organized as follows: In Section 2, the numerical model is presented. In Section 3, the analytical model is presented. In Section 4, simulation results are presented and compared to the experimental results. Discussions are made in this section. In Section 5 conclusions are completed.

2. Numerical Model

2.1 Governing equations

Figure 2 shows a schematic diagram of the calculation domain, including the substrate, melt pool, remelted zone, deposited layer and part of the gas region. In the laser deposition process, melting and solidification cause the phase transformation at the solid/liquid interface. A mushy zone containing solid and liquid is formed. In this study the continuum model [1, 2] is adopted to derive the governing equations.
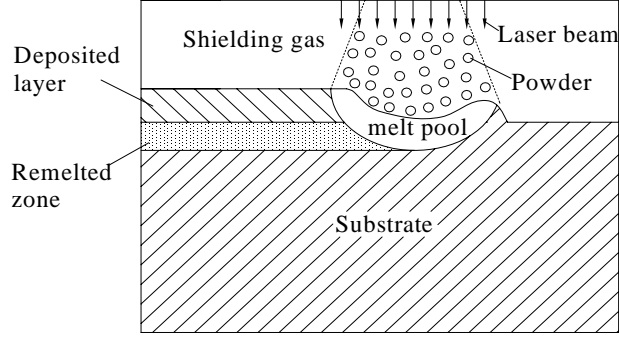
Fig. 2. Schematic of the calculation domain

The assumptions for the system of governing equations include: (1) the fluid flow in the melt pool is a Newtonian, incompressible, laminar flow; (2) the solid and liquid phases in the mushy zone are in local thermal equilibrium; (3) the solid phase is rigid; and (4) isotropic permeability exists. For the system of interest, the conservation equations for mass, momentum and energy are summarized as follows:

Continuity

$$\frac{\partial \rho}{\partial t} + \nabla \cdot (\rho \vec{V}) = 0 \tag{1}$$

Momentum

$$\frac{\partial}{\partial t}(\rho \vec{V}) + \nabla \cdot (\rho \vec{V} \vec{V}) = \nabla \cdot (\mu_l \frac{\rho}{\rho_l} \nabla \vec{V}) - \nabla p - \frac{\mu_l}{K}\frac{\rho}{\rho_l}(\vec{V} - \vec{V}_s) + \rho \vec{g} + S \tag{2}$$

Energy

$$\frac{\partial (\rho h)}{\partial t} + \nabla \cdot (\rho \vec{V} h) = \nabla \cdot (k \nabla T) - \nabla \cdot (\rho (h_l - h)(\vec{V} - \vec{V}_s) \tag{3}$$

In equations (1)-(3), the continuum density, specific heat, thermal conductivity, vector velocity, and enthalpy are defined as follows:

$$\rho = g_s \rho_s + g_l \rho_l \qquad c = f_s c_s + f_l c_l \qquad k = g_s k_s + g_l k_l$$

$$\vec{V} = f_s \vec{V}_s + f_l \vec{V}_l \qquad h = f_s h_s + f_l h_l \tag{4}$$

The liquid fraction temperature relationship is given by:

$$g_l = \begin{cases} 0 & \text{if } T < T_s \\ \dfrac{T - T_s}{T_l - T_s} & \text{if } T_s \leq T \leq T_l \\ 1 & \text{if } T > T_l \end{cases} \qquad (5)$$

The other volume and mass fractions can be obtained by:

$$f_l = \frac{g_l \rho_l}{\rho} \qquad f_s = \frac{g_s \rho_s}{\rho} \qquad g_s + g_l = 1 \quad f_s = 1 - f_l \qquad (6)$$

The phase enthalpy for the solid and the liquid can be expressed as:

$$h_s = \int_0^T c_s(T)dT \qquad h_l = \int_0^{T_s} c_s(T)dT + \int_{T_s}^T c_l(T)dT + L_m \qquad (7)$$

where L_m is the latent heat of melting.

Permeability, K, is assumed to vary with liquid volume fraction according to the Carman - Kozeny equation[3] derived from Darcy's law:

$$K = \frac{g_l^3}{C(1 - g_l)^2} \qquad (8)$$

where the parameter C is a constant depending on the morphology and size of the dendrites in the mushy zone. The S is a source term that will be defined in Section 2.4.

2.2 Tracking of the solid/liquid interface

The solid/liquid interface is implicitly tracked by the continuum model [1, 2]. In the solid phase region and liquid phase region, the third term on the right-hand side of Eq. (2) vanishes. This is because in the solid phase region $\vec{V} = \vec{V}_s = 0$ and in liquid phase region K→∞ since $g_l = 1$. So this term is only valid in the mushy zone.

2.3 Tracking of the free surface

The liquid/vapor interface, or the free surface of the melt pool, is very complex due to surface tension, thermocapillary force, and impaction of the powder injection. In this study, the

Volume-Of-Fluid (VOF) method [4] is employed to track the evolution of the moving free surface of the melt pool. The melt pool configuration is defined in terms of a volume of fluid function, F(x,y,t), which represents the volume of fluid per unit volume and satisfies the conservation equation:

$$\frac{\partial F}{\partial t} + (V \cdot \nabla)F = 0 \tag{9}$$

2.4 Formulation of source term

The source term, S, in the momentum equation is contributed by the interface forces acting on the free surface, such as surface tension, etc. In this study, the continuum surface force (CSF) model [5] is used to reformulate the surface force. In its standard form, surface tension is formulated as [5]:

$$\vec{F}_s(\vec{x}_s) = \hat{n}\gamma\kappa + \nabla_S\gamma \tag{10}$$

where $\vec{F}_s(\vec{x}_s)$ is the net surface force at a point $\vec{x}_s$ on a interface S. $\hat{n}$ is a unit normal to S at the point $\vec{x}_s$, which is given by:

$$\hat{n} = \frac{\vec{n}}{|\vec{n}|} \tag{11}$$

where $\vec{n}$ is the surface normal vector and can be computed from the gradient of the VOF function:

$$\vec{n} = \nabla F \tag{12}$$

∇_S is the gradient along a direction tangential to the interface, which is defined as:

$$\nabla_S = \nabla - \nabla_N = \nabla - \hat{n}(\hat{n} \cdot \nabla) \tag{13}$$

γ and κ represent surface tension coefficient and curvature, respectively. κ is given in [6]:

$$\kappa = -(\nabla \cdot \hat{n}) = \frac{1}{|\vec{n}|}\left[(\frac{n}{|\vec{n}|} \cdot \nabla)|\vec{n}| - (\nabla \cdot \vec{n}) \right] \tag{14}$$

By using the CSF model, the surface force $\vec{F}_s$ is reformulated into a volume force $\vec{F}_b$ as follows:

$$\vec{F}_b = \vec{F}_S|\vec{n}|\frac{F}{\langle F \rangle} = \vec{F}_S|\nabla F|\frac{F}{\langle F \rangle} \tag{15}$$

where $\langle F \rangle$ is the averaged F value across the free surface. Thus, the source term S in equation (2) is formulated as:

$$S = (\vec{n}\gamma\kappa + \nabla_S\gamma)|\nabla F|\frac{F}{\langle F \rangle} \tag{16}$$

2.5 Boundary Conditions

The boundary conditions at the free surface satisfie the following equation:

$$k\frac{\partial T}{\partial n} = \frac{\eta(P_{laser} - P_{atten})}{\pi R^2} - h_c(T - T_\infty) - \varepsilon\sigma(T^4 - T_\infty^4) - \dot{m}_e L_v \tag{17}$$

where terms on the right-hand side are laser irradiation, convective heat loss, radiation heat loss and evaporation heat loss, respectively. P_{laser} is the power of laser beam, P_{atten} the power attenuated by the powder cloud, R is the laser beam radius, η the laser absorption coefficient. P_{atten} is calculated according to Frenk's et al. model [7] with a minor modification:

$$P_{atten} = P_{laser}\left[1 - \exp\left(-\frac{3Q_{ext}\dot{m}l}{\pi\rho r_p D_{jet}v_p}\right)\right] \tag{18}$$

where $\dot{m}$ denotes the powder mass flow rate, l is the stand-off distance from the nozzle exit to the substrate, ρ is powder density, r_p is the radius of the powder particle, D_{jet} is the diameter of the powder jet, v_p is the powder injection velocity, and Q_{ext} is the extinction coefficient. It is assumed that the extinction cross section is close to the actual geometrical cross section, and Q_{ext} takes a value of unity. In the evaporation term, $\dot{m}_e$ is the evaporation mass flux and L_v is the latent heat of evaporation. According to Choi et al.'s "overall evaporation model" [8], $\dot{m}_e$ is of the form:

$$\log\dot{m}_e = A + 6.1210 - \frac{18836}{T} - 0.5\log T \tag{19}$$

where A is a constant dependent on the material.

The boundary conditions at the bottom, left and right wall satisfy the following equations:

$$k \frac{\partial T}{\partial n} = -h_c (T - T_\infty) \tag{21}$$

$$u = 0 \qquad v = 0 \tag{22}$$

2.6 Powder injection

Powder particles that inject onto the top surface can be classified into three categories. (1) Those powder particles that have not been melted during their passage and hit the solid part of the substrate will deflect and lose. (2) Those powder particles that have been melted before they arrive on the substrate and impact the solid part of the substrate will stick to the surface of the substrate. (3) Those powder particles that fall into the melt pool including melted and unmelted will merge and mix with the molten liquid in the melt pool [9]. In this study, the powder particles belonging to the last two cases will be utilized.

2.7 Numerical algorithm

The governing equations (Eq. (1)-(3), and (10)) and all related supplemental equations and boundary conditions are solved through the following iterative scheme:

1. Equation (1)-(2) and the related boundary conditions are solved iteratively using the SOLA-VOF algorithm [10] to obtain velocities and pressures. At each time step, the discretized momentum equations calculate new velocities in terms of an estimated pressure field. Then the pressure field is iteratively adjusted and velocity changes induced by each pressure correction are added to the previous velocities. This iterative process is repeated until the continuity equation is satisfied under an imposed tolerance by the newly computed velocities.

2. The energy equation (4) is solved by an implicit method.

3. Equation (10) is solved to obtain the updated free surface and geometry of the melt pool.

4. Advance to the next time step and back to step 1 until the desired process time is reached.

In this scheme, staggered grids are employed where the temperatures, pressures and VOF function are

located at the cell center and the velocities at the walls. The source term in the momentum is obtained

at grid points that are located in the transition region. A fixed grid is used with the mesh size of 10μm,

which is proved to achieve grid independence. The time step is taken at the level of 10^{-6}s initially and

adapted subsequently according to the convergence and stability requirements of the SOLA-VOF

algorithm [10], the CSF model [5], and the numerical solution for the energy equation.

3. Analytical Model

In this paper the analytical solution for the temperature distribution in preheating of the substrate is

based on Komanduri and Hou's work [11], which is based on moving heat source theory of Jaeger

[12] and Carslaw and Jaeger [13].

3.1 Solution of a disc heat source with a uniform intensity distribution, moving on the surface of a semi-infinite medium

Follow Komanduri and Hou's work [11], the temperature rise of a point M(x, y, z) at any time t after

the initiation of the heat source in a semi-infinite medium due to a disc heat source is given by:

$$\Delta T = \frac{P}{2c\rho(4\pi\alpha)^{3/2}} \int_0^t \frac{d\tau}{\tau^{3/2}} \exp(-\frac{r_0^2 + X^2 + y^2 + z^2}{4\alpha\tau}) \cdot \exp(-\frac{Xv}{2\alpha}) \cdot \exp(-\frac{v^2\tau}{4\alpha}) \cdot I_0(\frac{r_o}{2\alpha\tau}\sqrt{(X+v\tau)^2 + y^2}) \quad (23)$$

where y, z are coordinates in the absolute coordinate system, while X is the corresponding moving

coordinate. P is the laser power absorbed by the substrate. r_0 is the radius of the disc heat source, v its

moving velocity, I_0 the modified Bessel function of the first kind, order zero. c, ρ, α are specific heat,

density and thermal diffusivity, respectively. Let $R^2 = r_0^2 + X^2 + y^2 + z^2$, Eq. (23) becomes:

$$\Delta T = \frac{P}{2c\rho(4\pi\alpha)^{3/2}} \int_0^t \frac{d\tau}{\tau^{3/2}} \exp(-\frac{R^2}{4\alpha\tau}) \cdot \exp(-\frac{Xv}{2\alpha}) \cdot \exp(-\frac{v^2\tau}{4\alpha}) \cdot I_0(\frac{r_o}{2\alpha\tau}\sqrt{(X+v\tau)^2 + y^2}) \quad (24)$$

3.2 Solution of a disc heat source with a uniform intensity distribution, considering the boundary conditions of the bottom and side surfaces

Here the bottom and side surfaces are considered as adiabatic. Using the image method, nine image

heat sources are considered. The temperature rise at any point M is the sum of the effects from all the

primary and the image heat sources which are located away from the point M at distances of R_0, R_1,

R_2, R_3, R_4, R_5, R_6, R_7, R_8, R_9, respectively.   Suppose the substrate has the dimensions $H \times L \times W$, H

is the height of the substrate, L is the length of substrate in the heat source moving direction. The

values of these distances and their projections on the X-axis are given in Table 1.

Table 1 Distances and their projections

Symbol of	Value of Distance	Symbol of	Value of Projection
R_0	$\sqrt{X^2 + y^2 + z^2}$	X_0	X
R_1	$\sqrt{X^2 + y^2 + (2H - z)^2}$	X_1	X
R_2	$\sqrt{(X + 2vt)^2 + y^2 + z^2}$	X_2	$-(X + 2vt)$
R_3	$\sqrt{(X + 2vt)^2 + y^2 + (2H - z)^2}$	X_3	$-(X + 2vt)$
R_4	$\sqrt{(2(L - vt) - X)^2 + y^2 + z^2}$	X_4	$2(L - vt) - X$
R_5	$\sqrt{(2(L - vt) - X)^2 + y^2 + (2H - z)^2}$	X_5	$2(L - vt) - X$
R_6	$\sqrt{X^2 + (y + W)^2 + z^2}$	X_6	X
R_7	$\sqrt{X^2 + (y + W)^2 + (2H - z)^2}$	X_7	X
R_8	$\sqrt{X^2 + (y + W)^2 + z^2}$	X_8	X
R_9	$\sqrt{X^2 + (y + W)^2 + (2H - z)^2}$	X_9	X

The temperature rise at any point M caused by the primary heat source is given by Eq. (24), and the

temperature rise at any point M caused by each of the image heat source is obtained by substituting

the aforementioned values of the distances and their relevant projections on the X-axis instead of R

and X in Eq. (24).

4. Numerical Simulation and Experiments

4.1 Numerical simulation

Simulation is performed based on the capability of our experimental facilities to compare the

simulation results with the experimental measurements. A continuous wave diode laser with an 808 nm wavelength is considered as the energy source. The laser intensity distribution is uniform. For substrates, Ti-6Al-V4 plates with a thickness of 0.25 inch are selected. Ti-6Al-V4 powder particles with a diameter from 40 to 140 μm are used as deposit material. The laser absorption coefficient is measured by Sparks et al. [14]. The material properties and the main process parameters are shown in Table 2. Figure 2 shows the typical simulation results for temperature, velocity and VOF function.
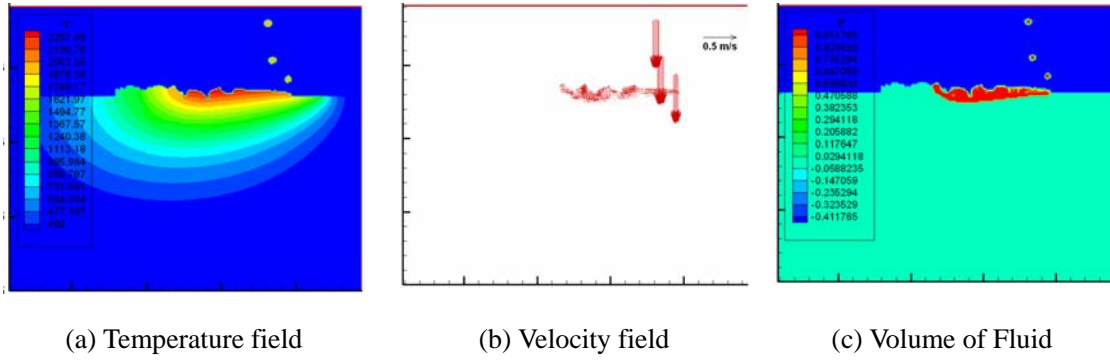

    (a) Temperature field   (b) Velocity field   (c) Volume of Fluid

Fig. 2. Simulation results at t = 130 ms (laser power-910W, travel speed- 20ipm, powder mass flow rate-4.68g/min)

4.2 Experiments

The experiments were performed on the LAMP system shown in Fig. 3. The system consists of a diode laser, powder delivery unit, 5-axis CNC machine, and monitoring subsystem. The laser system used in the study was Nuvonyx (Nuvonyx Inc.) ISL-1000M Laser Diode System which combines state-of-the-art micro-optics with laser diodes to produce the only single wavelength fiber coupled direct diode laser at power levels up to 1000 watts CW. The laser emits at 808 nm and operates in the continuous wave (CW) mode. To protect oxidization of Ti-6Al-V4, the system is covered in an environmental chamber to supply argon gas for titanium deposition. For the other aspects of the system architecture, refer to Liou et al. [15] and Boddu et al.[16]. The substrates have dimensions of 2.5×2.5×0.4 in. The Ti-6Al-4V samples were irradiated using a laser beam with a beam spot diameter of 2.5 mm.

Table 1. Material properties for Ti-6Al-4V and main process parameters

Nonmenclature	Symbol	Value (unit)
Melting temperature	T_m	1900.0K
Liquidus temperature	T_l	1923.0K
Solidus temperature	T_s	1877.0K
Evaporation temperature	T_v	3533.0K
Solid specific heat at constant pressure [17]	c_{ps}	$\begin{cases} 483.04 + 0.215T & T \leq 1268K \\ 412.7 + 0.1801T & 1268 < T \leq 1923 \end{cases} J/kg\ K$
Liquid specific heat at constant pressure [18]	c_{pl}	831.0 J/kg K
Thermal conductivity [17]	k	$\begin{cases} 1.2595 + 0.0157T & T \leq 1268K \\ 3.5127 + 0.0127T & 1268 < T \leq 1923 \\ -12.752 + 0.024T & T > 1923 \end{cases} W/m\ K$
Solid density [18]	ρ_s	4420 – 0.154 (T – 298 K)
Liquid density [18]	ρ_l	3920 – 0.68 (T – 1923 K)
Latent heat of fusion [18]	L_m	2.86×10^5 J/kg
Latent heat of evaporation	L_v	9.83×10^6 J/kg
Dynamic viscosity	μ	3.25×10^{-3} N/m s (1923K) 3.03×10^{-3} (1973K) 2.66×10^{-3} (2073K) 2.36×10^{-3} (2173K)
Radiation emissivity [19]	ε	$0.1536 + 1.8377 \times 10^{-4}$ (T - 300.0 K)
Laser absorption coefficient [14]	η	0.4
Powder particle diameter	D_p	40-140 μm
Shielding gas pressure	P_g	5 psi
Ambient temperature	T_∞	300K
Convective coefficient	h_c	10 W/m^2 K

In order to validate the model predictions, single path deposition experiments are conducted. The comparisons between model predictions and experimental results are conducted in terms of melt pool peak temperature. The melt pool peak temperature is calibrated through the dual-wavelength non-contact temperature sensor, which can effectively decrease the disturbance from the powder and other dusts.
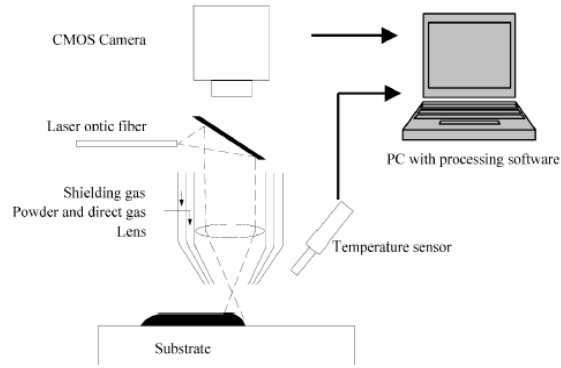
Fig. 3. Schematic of experimental setup

4.3 Comparisons and discussions

Fig. 4 and Fig. 5 show the comparisons between experimental measurements and model predictions. Fig. 4 shows the effects of laser power on melt pool peak temperature. It can be seen that an increase in the laser power will increase the melt pool temperature. This is easy to understand. As the laser power increases, more power is available for melting the substrate. Fig. 4 shows the effects of laser scanning speed on the melt pool peak temperature. An increase in the laser scanning speed will decrease the melt pool peak temperature. This is because, as scanning speed decreases, the laser material interaction time is extended.

From Fig. 4-5, we can see that the general trend between experimental measurements and model predictions is consistent. At different power intensity level, there is a different error from 10 K (about 0.5%) to 121K (about 5%). It can be seen that at a higher power intensity level, there is a bigger error between measurements and predictions. This is because the numerical model is two-dimensional. It doesn't consider the heat and mass transfer in the third direction. At a higher power intensity level, heat and mass transfer in the third dimension is more significant.

The errors between experimental measurements and model predictions are analyzed to mainly come from the following aspects: (1)The two-dimensional nature of the numerical model; (2)The thermo-physical properties taken for the analytical model; (3) The uncertainties of the material

13

properties and the appropriateness of the sub-models for the numerical model; (4) Boundary conditions. Adiabatic boundary conditions are assumed in the analytical model and the numerical model for the bottom surface and side surfaces. Measurements also have been taken to achieve such boundary conditions in experiments. But it is hard to get absolute adiabatic boundary conditions.
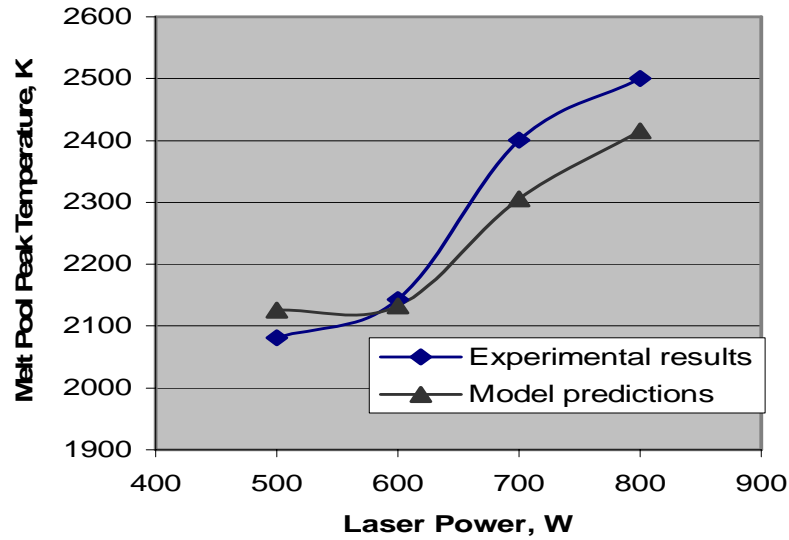

Fig. 4 Comparisons between experimental measurements and model predictions at a constant powder mass flow rate of 5g/min and a constant laser scanning speed of 20 inch/min. (For actual deposition)
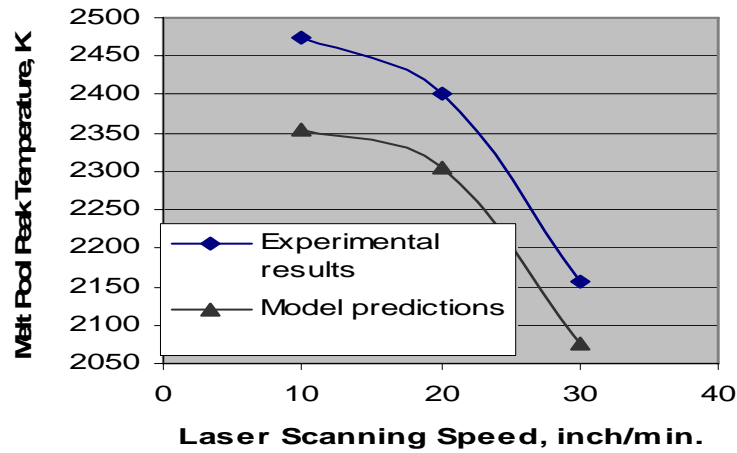

Fig. 5 Comparisons between experimental measurements and model predictions at a constant powder mass flow rate of 5g/min and a constant laser power of 700 W. (For actual deposition)

5. Conclusions

An analytical model for thermal analysis of temperature rise due to a moving heat source is combined into a comprehensive heat transfer and fluid flow numerical model for the laser deposition process. The analytical model is used for the preheating process before the actual laser deposition with powder injection. And the numerical model is used for the actual laser deposition process. Thus the outputs of the analytical model are used as the inputs of the numerical model. Experiments have been done to validate the model predictions. A consistent general trend is found between experimental measurements and the model predictions. The sources of the errors have been analyzed.

Acknowledgements

References

[1] W.D. Bennon, F.P. Incropera, A continuum model for momentum, heat and species transport in binary solid-liquid phase change systems-I. model formulation, International Journal of Heat and Mass Transfer 30 (1987) 2161-2170.

[2] W.D. Bennon, F.P. Incropera, A continuum model for momentum, heat and species transport in binary solid-liquid phase-change systems--II. Application to solidification in a rectangular cavity, International Journal of Heat and Mass Transfer 30 (1987) 2171-2187.

[3] P.C. Carman, Fluid flow through granular beds, Trans. Institution Chem. Engrs. 15 (1937) 150-166.

[4] C.W. Hirt, B.D. Nichols, Volume of fluid (VOF) method for the dynamics of free boundaries, Journal of Computational Physics 39 (1981) 201-225.

[5] J. U. Brackbill, D. B. Kothe, C. Zemach, A continuum method for modeling surface tension, Journal of Computational Physics 100 (1992) 335-354.

[6] C. Prakash, V. Voller, On the numerical solution of continuum mixture model equations describing binary solid-liquid phase change, Numerical Heat Transfer 15B (1989) 171-89.

[7] A. Frenk, M. Vandyoussefi, J. Wagniere, A. Zryd, W. Kurz, Analysis of the laser-cladding process for stellite on steel, Metallurgical and Materials Transactions B (USA) 28B (1997) 501-508.

[8] M. Choi, R. Greif, M. Salcudean, A study of the heat transfer during arc welding with applications to pure metals or alloys and low or high boiling temperature materials, Numerical Heat Transfer 11 (1987) 477-491.

[9] L. Han, F.W. Liou, K.M. Phatk, Modeling of laser cladding with powder injection, Metallurgical and Materials Transactions B 35B (2004) 1139-1150.

[10] B. D. Nichols, C.W. Hirt, R. S. Hotchkiss, SOLA-VOF: A solution algorithm for transient fluid flow with multiple free boundaries,LA-8355, Los Alamos National Laboratory.

[11] R.Komanduri, Z.B. Hou, Thermal analysis of the arc welding process. I. General solutions, Metallurgical and Materials Transactions B (USA). Vol. 31B, no. 6, pp. 1353-1370B, 2000

[12] J.C. Jaeger, Proc. R. Soc. NSW, 1942, vol. 76, 203-224

[13] H.S. Carslaw, J.C. Jaeger, Conduction of Heat in Solids, 2nd ed., Oxford University Press, Oxford, United Kingdom,1959

[14] Todd E. Sparks, Zhiqiang Fan, Measurement of laser absorption coefficient of several alloys for diode laser, unpublished report, 2006.

[15] F. Liou, J. Choi, R. Landers, V. Janardhan, S. Balakrishnan, S. Agarwal, Proc.12th Annual Solid Freeform Fabrication Symp., Austin, TX, Aug. 6–8, 2001, pp. 138-45.

[16] M. Boddu, S. Musti, R. Landers, S. Agarwal, F. Liou, Proc. 12th Annual Solid Freeform Fabrication Symp., Austin, TX, Aug. 6–8, 2001, pp. 452-59.

[17] S.M. Kelly, Thermal and microstructure modeling of metal deposition processes with application to Ti-6Al-4V, Ph.D. thesis, Virginia Polytechnic Institute and State University, 2004.

[18] K. C. Mills, Recommended values of thermophysical properties for selected commercial alloys, Woodhead, Cambridge, 2002.

[19] Tobias Lips, Bent Fritsche, A comparison of commonly used re-entry analysis tools, Acta Astronautica 57 (2005) 312-323.